To cite this version :

Pierre GILORMINI, Francisco CHINESTA - Viscous drag and rod orientation kinematics in an orthotropic fluid - Journal of Non-Newtonian Fluid Mechanics - Vol. Volume 270, p.Pages 96-103 - 2019

Viscous drag and rod orientation kinematics in an orthotropic fluid

Pierre Gilormini, Francisco Chinesta*

Laboratoire PIMM, Arts et Métiers, CNRS, CNAM, Hesam University, 151 Boulevard de l'Hôpital, Paris 75013, France

ARTICLE INFO

ABSTRACT

A model is proposed, where the evolution of the orientation of each fiber is coupled to the orientations of the surrounding fibers in the flow of a fiber-filled fluid and includes the effects of the fiber volume fraction and aspect ratio. This is performed by accounting for the effective behavior of the fiber-filled fluid, which is anisotropic although the fibers are embedded in an isotropic Newtonian fluid. The rotation of a fiber in these conditions is predicted by a dumbbell model, which allows an extension of Jeffery's equation to anisotropic cases. This involves the numerical evaluation of the drag force applied on a sphere in an orthotropic incompressible fluid, which is evaluated by finite element simulations. A simple fit is proposed for the practical use of the coupled model, which is applied finally to the orientation kinematics of a population of fibers in a simple shear flow, and the results are compared with the ones given by the standard uncoupled approach.

1. Introduction

In our former works we addressed the kinematics of rods, simulating short rigid straight fibers involved in reinforced plastics, by assimilating them to dumbbells with hydrodynamic forces applied on the dumbbell beads [1]. Such a modeling framework allows recovering the Jeffery equation for a prolate spheroid with infinite aspect ratio [2], as shown below. This rationale has been extended to study rigid [3] and deformable [4] clusters composed of rods, to address confinement effects [5,6], to include higher-order gradients [7], to consider viscoelastic surrounding fluids [8], or to account for rods inertia [9]. Moreover, in [3] the authors proved that the Jeffery equation for general ellipsoids is recovered by using a rigid tri-dumbbell analog. All these developments leading to the equivalence between ellipsoids and dumbbells were performed under the assumption that the particle is immersed in an isotropic fluid. When the particles volume fraction increases, the so-called semi-dilute regime is reached, where direct contacts between fibers can still be neglected but hydrodynamic interactions come into play as referred in the papers above (and the abondant references therein) or as addressed within a thermodynamic setting in [10]. This induces an anisotropic effective behavior of the fluid surrounding a particle and should alter its orientation kinematics, which is expected to deviate from the standard Jeffery prediction.

To our knowledge, the effects of this anisotropy on the rod kinematics has never been addressed, and all theories and models giving the orientation kinematics rely on an isotropic environment, in opposition with what is expected from self-consistent approaches, for instance. Therefore, the present work aims at developing an approximate model for the rotation of rigid spheroids with large aspect ratios (representing slender rods and fibers accurately) that takes into account the effective fluid behavior resulting from a population of fibers with a non-isotropic distribution of orientations. Since no analytical solution is available in the anisotropic case for the problem solved by Jeffery in isotropic conditions, a slender spheroid will first be assumed equivalent to a dumbbell, the orientation kinematics will be solved for the latter in the anisotropic case, and a direct comparison with a finite element simulation will validate the equivalence with a slender spheroid. Finally, the model will be applied to the orientation kinematics of a whole population of fibers suspended in a fluid submitted to a simple shear in order to emphasize the effects of taking anisotropy into account in the flow of fiber-filled plastics.

2. Rod kinematics in an anisotropic medium

To derive the dumbbell-based model, we start by revisiting the kinematics of a slender rod of length $2L$ immersed in an isotropic Newtonian fluid with viscosity η, where the kinematics described by the velocity field $\mathbf{v}(\mathbf{x})$ is assumed unperturbed by the presence of the rod, whatever its orientation. The latter is defined by the unit vector $\mathbf{p}$, and inertia effects are neglected in the sequel. If we assume the rod can be represented by the dumbbell depicted in Fig. 1 and that hydrodynamic forces apply on the two (identical) beads only, each being proportional to the difference between the velocity of the fluid $\mathbf{v}_0 + \nabla\mathbf{v}\,\mathbf{p}L$ (with $\mathbf{v}_0$ the velocity of the fluid at the dumbbell centroid G) and the velocity of the bead $\mathbf{v}_G + \dot{\mathbf{p}}L$ (with $\mathbf{v}_G$ the velocity of the dumbbell centroid), the force acting on the bead at $\mathbf{p}L$ (the origin of coordinates is taken at G) reads
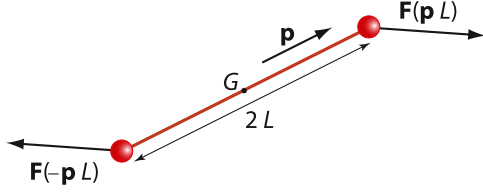
Fig. 1. Hydrodynamic forces applied on a dumbbell immersed in a Newtonian fluid.

$$\mathbf{F}(\mathbf{p}L) = \zeta(\mathbf{v}_0 + \nabla\mathbf{v}\,\mathbf{p}L - \mathbf{v}_G - \dot{\mathbf{p}}L), \tag{1}$$

where ζ is the drag coefficient in the isotropic fluid, and the force on the opposite bead at $-\mathbf{p}L$ is

$$\mathbf{F}(-\mathbf{p}L) = \zeta(\mathbf{v}_0 - \nabla\mathbf{v}\,\mathbf{p}L - \mathbf{v}_G + \dot{\mathbf{p}}L). \tag{2}$$

Adding these two forces and enforcing the linear momentum balance $\mathbf{F}(\mathbf{p}L) + \mathbf{F}(-\mathbf{p}L) = \mathbf{0}$ leads to $\mathbf{v}_0 = \mathbf{v}_G$, that is, the dumbbell centroid moves with the unperturbed fluid velocity. As the resulting torque must also vanish, the only possibility is that the forces act along the direction of $\mathbf{p}$, that is $\mathbf{F}(\mathbf{p}L) = \lambda\,\mathbf{p}$, with λ a real number:

$$\lambda\,\mathbf{p} = \zeta\,L(\nabla\mathbf{v}\,\mathbf{p} - \dot{\mathbf{p}}). \tag{3}$$

Taking the scalar product of both sides with $\mathbf{p}$ provides the λ value:

$$\lambda = \zeta\,L\,\mathbf{p}^T\nabla\mathbf{v}\,\mathbf{p}, \tag{4}$$

since $\mathbf{p}^T\mathbf{p} = 1$ and consequently $\mathbf{p}^T\dot{\mathbf{p}} = 0$, and (3) gives

$$\zeta\,L(\mathbf{p}^T\nabla\mathbf{v}\,\mathbf{p})\mathbf{p} = \zeta\,L(\nabla\mathbf{v}\,\mathbf{p} - \dot{\mathbf{p}}) \tag{5}$$

leading finally to the rotation rate of the dumbbell:

$$\dot{\mathbf{p}} = \nabla\mathbf{v}\,\mathbf{p} - (\mathbf{p}^T\nabla\mathbf{v}\,\mathbf{p})\mathbf{p} \tag{6}$$

which coincides with the well known Jeffery's equation for a rigid spheroid with an infinite aspect ratio. Therefore, the rotation of a slender fiber in an isotropic Newtonian fluid is equal to the rotation of a rigid dumbbell, and this remarkable coincidence, which was unrecognized in the early papers where rigid dumbbells were studied (see [11], for instance), has been stressed in [1].

It may be noticed that the drag coefficient is absent in (6), but this does not apply when the fluid is anisotropic, as we show now. In this case, the drag force is not necessarily aligned with the velocity of the bead with respect to the fluid, unless possibly along a symmetry axis of the fluid behavior, and an anisotropic drag tensor ζ is introduced, similarly to what has been done in [12]. This second-order tensor is positive definite, so that the drag force does dissipate energy, and therefore it has an inverse. The hydrodynamic force acting on the bead at $\mathbf{p}L$ reads now

$$\mathbf{F}(\mathbf{p}L) = \zeta(\mathbf{v}_0 + \nabla\mathbf{v}\,\mathbf{p}L - \mathbf{v}_G - \dot{\mathbf{p}}L), \tag{7}$$

and, taking into account the positivity of ζ, $\mathbf{v}_0 = \mathbf{v}_G$ yields again from the linear momentum balance. The angular momentum balance implies

$$\zeta(\nabla\mathbf{v}\,\mathbf{p}\,L - \dot{\mathbf{p}}\,L) = \lambda\,\mathbf{p}, \tag{8}$$

which, using the invertibility of ζ, can also be written as

$$\nabla\mathbf{v}\,\mathbf{p} - \dot{\mathbf{p}} = \frac{\lambda}{L}\,\zeta^{-1}\mathbf{p}. \tag{9}$$

Taking the scalar product with $\mathbf{p}$ gives

$$\mathbf{p}^T\nabla\mathbf{v}\,\mathbf{p} = \frac{\lambda}{L}\,\mathbf{p}^T\zeta^{-1}\mathbf{p}, \tag{10}$$

which leads to the value of λ:

$$\lambda = L\,\frac{\mathbf{p}^T\nabla\mathbf{v}\,\mathbf{p}}{\mathbf{p}^T\zeta^{-1}\mathbf{p}} \tag{11}$$

that can be introduced into (9) and gives finally

$$\dot{\mathbf{p}} = \nabla\mathbf{v}\,\mathbf{p} - \frac{\mathbf{p}^T\nabla\mathbf{v}\,\mathbf{p}}{\mathbf{p}^T\zeta^{-1}\mathbf{p}}\,\zeta^{-1}\mathbf{p}. \tag{12}$$

Since ζ^{-1} appears at both the numerator and denominator, it can be replaced by a normalized inverse drag tensor ξ where $\xi_{11} + \xi_{22} + \xi_{33} = 1$, so that

$$\dot{\mathbf{p}} = \nabla\mathbf{v}\,\mathbf{p} - \frac{\mathbf{p}^T\nabla\mathbf{v}\,\mathbf{p}}{\mathbf{p}^T\xi\,\mathbf{p}}\,\xi\,\mathbf{p} \tag{13}$$

generalizes (6). This expression for the rotation of a rigid dumbbell in an anisotropic fluid will be assumed below to govern also the rotation of a prolate spheroid with infinite aspect ratio. In this sense, this extends Jeffery's result to the anisotropic case.

Of course, (6) is recovered in the isotropic case, where the normalized inverse drag tensor reduces to $\xi = \delta/3$ (δ denotes the second-order identity tensor), because the drag tensor ζ simplifies to $\zeta\,\delta$. By taking the scalar product with $\mathbf{p}$, it may also be checked that (13) does satisfy the condition $\mathbf{p}^T\dot{\mathbf{p}} = 0$ to preserve the unit length of $\mathbf{p}$. Before comparing the kinematics (13) and (6) for a population of fibers, it is necessary to address three main issues: the effective behavior of the fiber-filled fluid must be detailed, the associated second-order ξ tensor must be computed, and the extension of (13) to a fiber must be validated. This is performed in the following Sections.

3. Orthotropic behaviors considered

The effective viscous behavior of a Newtonian fluid filled with fibers is deduced here by applying the Advani and Tucker [13] approach. This two-step procedure combines a model for the effective behavior when all fibers are aligned, and a closure relation applied to the symmetric second-order orientation tensor $\mathbf{a}$ otherwise. The latter is given by

$$\mathbf{a} = \int_{S(0,1)} \mathbf{p}\otimes\mathbf{p}\,\psi(\mathbf{p})\,\mathrm{d}\mathbf{p} \tag{14}$$

where the orientation distribution function $\psi(\mathbf{p})$, defined over the surface $S(0,1)$ of the unit ball, gives the fraction of fibers that are parallel to $\mathbf{p}$ and verifies the normality condition:

$$\int_{S(0,1)} \psi(\mathbf{p})\,\mathrm{d}\mathbf{p} = 1 \tag{15}$$

from which $a_{11} + a_{22} + a_{33} = 1$ results.

In the first step of the Advani–Tucker procedure, the Mori–Tanaka model [14], as reformulated by Benveniste [15], is used here for the case where all fibers are aligned and represented as very elongated prolate spheroids. This model was developed originally for composite materials, and was preferred by Tucker and Liang [16] at the end of their review of various models that predict the stiffness of short-fiber composites. Taking advantage of the formal equivalence between the equations governing the deformation of an elastic solid at small strain and those governing the flow at a given time in a linear viscous fluid at low Reynolds number (see [17], for instance), this model is extended readily to fiber-filled fluids. For a volume fraction f of aligned rigid fibers in an incompressible fluid of viscosity η, the effective behavior is transversely isotropic and defined by the following three material constants: an elongational viscosity

$$\eta_E = 3\left(1 + \frac{2}{3}\frac{f}{1-f}\frac{1-w^2}{h(w) - 2w^2 + 2h(w)w^2}\right)\eta \tag{16}$$

a longitudinal shear viscosity

$$\eta_L = \left(1 + 2\frac{f}{1-f}\frac{1-w^2}{(1+w^2)(2-3h(w))}\right)\eta \tag{17}$$

and a transverse shear viscosity

$$\eta_T = \left(1 + 4\frac{f}{1-f}\frac{1-w^2}{3h(w) - 2w^2}\right)\eta \tag{18}$$

where $w > 1$ denotes the fiber aspect ratio, and

$$h(w) = \frac{w}{(w^2-1)^{3/2}}\left(w\sqrt{w^2-1} - \text{arccosh } w\right).\qquad(19)$$

When $w \to \infty$, it may be noted that $h \to 1$ (with already $h \geq 0.99$ when $w \geq 16$), whereas $\eta_E \to \infty$ but both η_L and η_T tend to $(1+f)\eta/(1-f)$.

In the second step of the Advani-Tucker procedure, non-aligned fibers are considered, and an evaluation of the anisotropic fluid behavior is obtained by combining the above unidirectional case and information about the orientation distribution function. The latter is reduced to the second-order orientation tensor **a**, provided that a suitable closure relation is applied, which defines a fourth-order orientation tensor related to **a**. Here, the IBOF closure proposed by Chung and Kwon [18] is used, which has been developed by fitting over a large set of flow simulations and **a** values. As a result, the effective behavior is orthotropic, with its three material symmetry planes being normal to the principal axes of **a**. In the latter system of axes, six material parameters are defined for an incompressible orthotropic fluid behavior: three elongational viscosities η_{11}, η_{22} and η_{33}, and three shear viscosities η_{12}, η_{23} and η_{31}. These 6 parameters are deduced from the volume fraction f and aspect ratio w of the fibers (to get the reference unidirectional case), and from the **a** tensor (to include the orientation distribution) through the expressions given in [18]. The linear relation between the deformation rate **D** and the stress deviator **s** (or extra-stress, such that the stress tensor is given by $\boldsymbol{\sigma} = \mathbf{s} - p\,\boldsymbol{\delta}$, where p is a pressure) writes as follows in the principal axes of orthotropy (the reverse expressions for the components of **s** in terms of **D** are more involved):

$$D_{11} = \frac{s_{11}}{\eta_{11}} + \left(\frac{1}{\eta_{33}} - \frac{1}{\eta_{11}} - \frac{1}{\eta_{22}}\right)\frac{s_{22}}{2} + \left(\frac{1}{\eta_{22}} - \frac{1}{\eta_{33}} - \frac{1}{\eta_{11}}\right)\frac{s_{33}}{2}$$

$$D_{22} = \left(\frac{1}{\eta_{33}} - \frac{1}{\eta_{11}} - \frac{1}{\eta_{22}}\right)\frac{s_{11}}{2} + \frac{s_{22}}{\eta_{22}} + \left(\frac{1}{\eta_{11}} - \frac{1}{\eta_{22}} - \frac{1}{\eta_{33}}\right)\frac{s_{33}}{2}$$

$$D_{33} = \left(\frac{1}{\eta_{22}} - \frac{1}{\eta_{33}} - \frac{1}{\eta_{11}}\right)\frac{s_{11}}{2} + \left(\frac{1}{\eta_{11}} - \frac{1}{\eta_{22}} - \frac{1}{\eta_{33}}\right)\frac{s_{22}}{2} + \frac{s_{33}}{\eta_{33}}\qquad(20)$$

and $D_{12} = s_{12}/(2\eta_{12})$, $D_{23} = s_{23}/(2\eta_{23})$, $D_{31} = s_{31}/(2\eta_{31})$ for the shear components, in agreement with Beaussart et al. [17] using different notations. These relations are complemented by an objective evolution law for the **a** tensor, which includes the rotation of the orthotropy axes and induces an updating of the six viscosities through the Advani–Tucker model.

The special case of transverse isotropy about axis 1 that applies when all fibers are parallel is recovered when $\eta_{11} = \eta_E$, $\eta_{12} = \eta_{31} = \eta_L$, $\eta_{23} = \eta_T$, $\eta_{22} = \eta_{33} = 4\eta_E\eta_T/(\eta_E + \eta_T)$. In the limit isotropic case, where $a_{11} = a_{22} = a_{33} = 1/3$, one has $\eta_{11} = \eta_{22} = \eta_{33} = 3\eta_{12} = 3\eta_{23} = 3\eta_{31}$. The Abaqus [19] finite element code is employed in the simulations reported below, using again the equivalence between elastic solids and linear fluids, which requires the addition of three Poisson's ratios to the material constants. They were defined such that a Poisson's ratio of 0.5 minus 10^{-6} results in the isotropic case, which means that the incompressibility condition is approached extremely closely.

4. Viscous drag in orthotropic fluids

4.1. Preliminary validation tests

The drag of a sphere translating in an unbounded isotropic incompressible viscous fluid has been calculated in 1851 by Stokes in a famous paper [20], but an extension to the case of a finite domain has been performed by Lin et al. [21]. These authors have shown that when a sphere of radius R moves with velocity v at the center of a spherical fluid domain of radius qR, with zero velocity at the boundary, the drag force can be expressed in closed form:

$$F = 24\frac{q^5 + q^4 + q^3 + q^2 + q}{4q^5 - 5q^4 - 5q^3 + 5q^2 + 5q - 4}\pi R\eta v\qquad(21)$$

which recovers the well-known relation $F = 6\pi R\eta v$ derived by Stokes when $q \to \infty$. This result, which has been established originally for a
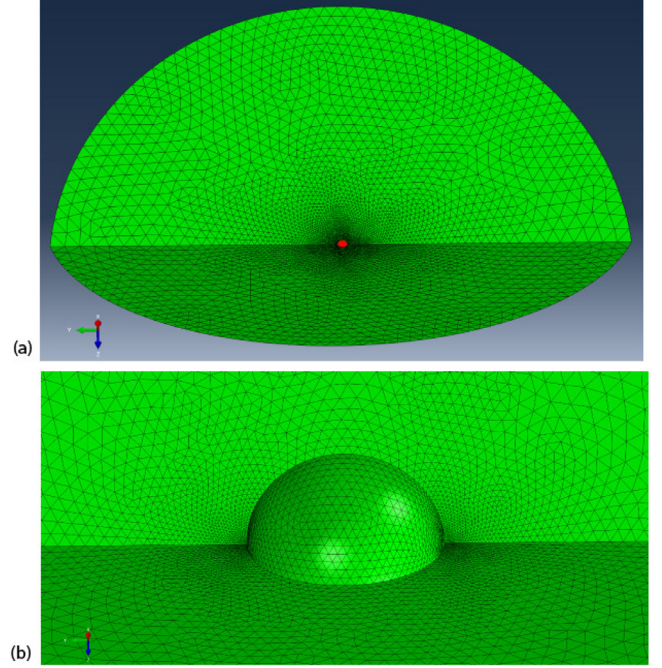

Fig. 2. (a) Mesh used in the finite element simulations to compute the viscous drag of a sphere moving in an orthotropic fluid. The sphere (in red), with a velocity parallel to the Y-axis (horizontal), is embedded in a 100 times larger fluid domain (in green), and one-fourth of the geometry is considered for symmetry reasons. (b) Enlarged view in the vicinity of the rigid moving sphere; to avoid meshing its volume, the velocities of all nodes at its surface are set equal and parallel to the Y-axis. (For interpretation of the references to colour in this figure legend, the reader is referred to the web version of this article.)

spherical inclusion displaced in a finite spherical elastic medium [21], implies that the drag force is 8% over Stokes' value when $q = 30$, over about 5% when $q = 50$, and still over 2% when $q = 100$. This is an indirect consequence of the slow r/R decrease of the velocity field in Stokes' solution, where r denotes the radial coordinate. Since a precise evaluation of the drag force in an unbounded orthotropic fluid is desired in this study, a mesh extending from the moving sphere up to 100 times its radius has been defined for the numerical simulations. More precisely, one fourth of the inner and outer spheres has been considered, which is bounded by symmetry planes (see Fig. 2a). The mesh has been generated with the Netgen mesh generator [22], it contains 607, 852 nodes, 493, 384 quadratic 10-node tetrahedral elements using a hybrid formulation (i.e., where the displacements and the pressure are degrees of freedom), which results in 2, 262, 943 unknowns. As shown in Fig. 2b, the mesh has been refined at the two points where a singularity is expected, i.e., where a streamline ends onto the moving sphere, for symmetry reasons.

A unit displacement of the central spherical surface has been prescribed along the Y axis, which corresponds to a unit velocity in terms of the elasticity-viscosity equivalence, whereas the surface of the outer sphere was fixed, and the resulting force has been computed with Abaqus. When the fluid is isotropic, with a unit η value, the computed force on a sphere of unit radius is 19.2827, whereas a value of 19.2831 is given by (21), i.e., 1.023 times Stokes' value. This very good agreement validates the mesh and the finite element approach for computing the drag force. Moreover, this suggests also that an error of about 2% might be expected when the drag of a sphere in an unbounded anisotropic fluid will be evaluated from simulations with a mesh of finite size extending up to 100 times the sphere radius. Nevertheless, the results for the components of the normalized inverse drag tensor may be even more precise, since ratios between drag forces in different directions are involved and errors may cancel out. For instance, the exact value of 1/3
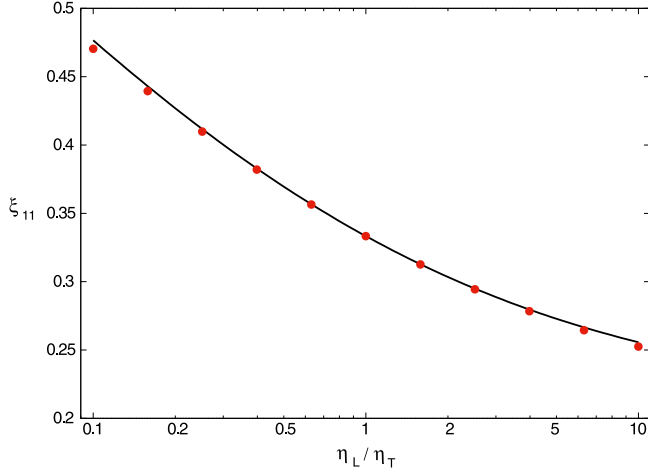
Fig. 3. Component of the normalized inverse drag tensor ξ parallel to the main symmetry axis of an incompressible transversely isotropic fluid where $\eta_E = 3\eta_T$. Finite element results (symbols) and analytical solution of Gómez-González and Álamo [23] (solid curve).

Fig. 4. Set of 45 (a_{11}, a_{22}) pairs used for the evaluation of the inverse drag tensor.

is obtained for each component in the isotropic case, although the drag force is overestimated by 2% in each direction.

Another validation of the finite element modeling is provided by comparing to the remarkable solution obtained by Gómez-González and del Álamo [23] for the viscous drag of a sphere in a transversely isotropic fluid. Actually, the results of Gómez-González and Álamo [23] have been obtained in the more general case of a nematic fluid, but the case of incompressible transverse isotropy is obtained for a special choice of the material variables: $\alpha_1 = 4(\eta_T - \eta_L)$, $\eta_a = \eta_T$ and $\eta_b = \eta_c = \eta_L$ in the notations of Gómez-González and Álamo [23]. This corresponds to an incompressible transversely isotropic fluid where $\eta_E = 3\eta_T$, with η_L/η_T left as a single anisotropy parameter, the isotropic case being recovered when $\eta_L/\eta_T = 1$. The quite complex expressions obtained for the drag force when the sphere is displaced either parallel ($\zeta_{\parallel}$) or perpendicular ($\zeta_{\perp}$) to the direction of transverse isotropy are not repeated here, but they can be found in [23]. They allow to compute the component of the normalized inverse drag tensor along the axis of transverse isotropy:

$$\xi_{11} = \frac{\zeta_{\perp}}{\zeta_{\perp} + 2\zeta_{\parallel}} \tag{22}$$

with $\xi_{22} = \xi_{33} = (1 - \xi_{11})/2$, so that $\xi_{11} + \xi_{22} + \xi_{33} = 1$. When the η_L/η_T ratio is varied from 0.1 to 10, the curve shown in Fig. 3 is obtained for ξ_{11}. The agreement between the finite element results (for a finite fluid domain) and the analytical solution (for an unbounded fluid domain) is quite good, and the discrepancy with respect to the analytical values is at most -1.3%.

4.2. Application to orthotropic fluids

The evaluation of the viscous drag of a sphere in an incompressible orthotropic fluid has already been addressed in the context of the dumbbell kinetic theory at the scale of the polymer molecule. Among ealy papers, Curtiss and Bird [12] introduced this concept, and Bird and Wiest [24] reviewed various empirical formulae. More recently, Azaiez [25] proposed a linear combination of the identity tensor (which applies to the isotropic case) and **a**, and the associated polymer-fiber interaction parameter has been fitted to experimental results by Guo et al. [26]. The concern here is the viscous drag at the upper scale of a fiber, modelled as a dumbbell, and a quantitative evaluation is sought by using finite element simulations.

In order to sample all possible **a** tensors for given fiber volume fraction and aspect ratio, a set of 45 points is defined in the classical triangle used by Cintra and Tucker [27], for instance, where $a_{11} \geq a_{22} \geq a_{33}$ (see
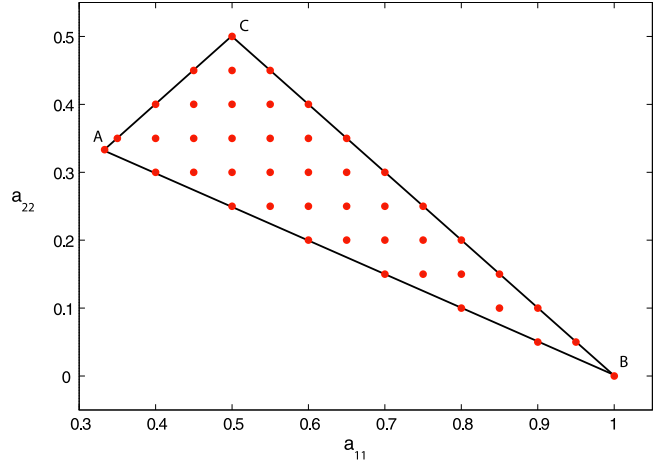
Fig. 4). This ordering of the principal values of **a** and the associated definition of axes (1,2,3) is kept from now on in this paper. Points A and B correspond to isotropic ($a_{11} = a_{22} = 1/3$) and unidirectional ($a_{11} = 1$) distributions of fiber orientations, respectively, lines AB and AC include the axisymmetric orientation distributions ($a_{22} = a_{33}$ along AB, $a_{11} = a_{22}$ along AC), and line BC is defined by $a_{33} = 0$. The 44 non-trivial (i.e., not corresponding to the isotropic case) points considered are aligned on a 0.05×0.05 grid, as shown in Fig. 4. Consequently, 132 finite element simulations are required for given fiber volume fraction and aspect ratio: one per translation of the sphere along each of the 3 principal directions of the orthotropic behavior associated with each of the 44 non-trivial points. Once the drag force (F_1, F_2, or F_3) has been evaluated along each of the principal axes of the **a** tensor, where the inverse drag tensor ξ also is diagonal, the normalized components of the latter are given by

$$\xi_{11} = \frac{1}{1 + \frac{F_1}{F_2} + \frac{F_1}{F_3}} \tag{23}$$

with a similar relation for ξ_{22}, and $\xi_{33} = 1 - \xi_{11} - \xi_{33}$. Since 5 volume fractions ($f = 0.1$, 0.15, 0.2, 0.25, and 0.3) were considered, and 5 aspect ratios ($w = 20$, 35, 50, 75, and 100) were used for each volume fraction, a total of 3,300 finite element simulations were performed.

No systematic simple trend could be found among the results, like $\xi_{11} \leq \xi_{22} \leq \xi_{33}$ for instance, or a component always increasing or decreasing when f or w increases. The expression proposed by Azaiez [25] for the inverse drag tensor, after normalization and using slightly different notations, namely

$$\xi = \frac{\sigma}{3}\delta + (1 - \sigma)\,\mathbf{a} \tag{24}$$

which recovers $\xi = \delta/3$ in the isotropic case ($\mathbf{a} = \delta/3$) whatever the value of σ, or for any **a** tensor if $\sigma = 1$, has been fitted to the set of results pertaining to fixed f and w values. In each case, 132 (a_{11}, ξ_{11}), (a_{22}, ξ_{22}), or (a_{33}, ξ_{33}) pairs (one set of three for each of the 44 non-trivial **a** tensors) were considered for determining the optimal σ value. Fig. 5a illustrates that the linear law (24) is quite acceptable in the favorable case of a low volume fraction ($f = 0.10$) of moderately elongated fibers ($w = 20$), but the agreement with the numerical results is less satisfactory in the more extreme case of a high volume fraction ($f = 0.30$) of very elongated fibers ($w = 50$) shown in Fig. 5b. Since a simple, though crude, law may nevertheless be useful in practice, the σ values obtained for the 25 combinations of f and w considered here are given in Table 1, which can be used to interpolate for intermediate fiber volume fractions f and aspect ratios w. It may be noted that σ increases when either f or w increases.
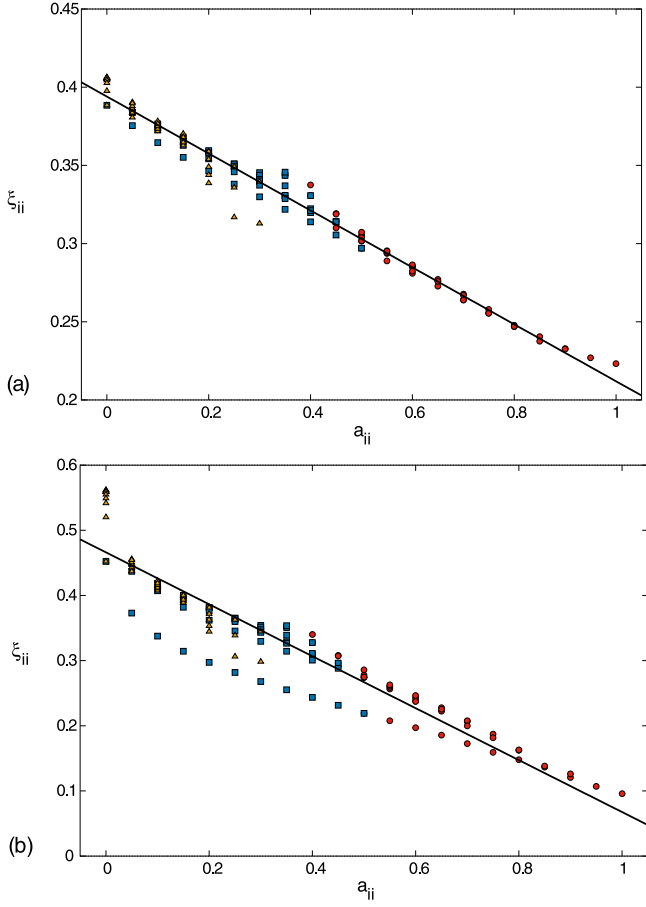
Fig. 5. Linear fit (straight line) obtained with the set of (a_{11}, ξ_{11}) (red circles), (a_{22}, ξ_{22}) (blue squares), and (a_{33}, ξ_{33}) (yellow triangles) pairs obtained for $f = 0.10$ and $w = 20$ (a), or for $f = 0.30$ and $w = 50$ (b). (For interpretation of the references to colour in this figure legend, the reader is referred to the web version of this article.)

Table 1
Values of the σ parameter obtained for various combinations of fiber volume fraction f and aspect ratio w.

	$f = 0.10$	$f = 0.15$	$f = 0.20$	$f = 0.25$	$f = 0.30$
$w = 20$	1.182	1.218	1.242	1.260	1.274
$w = 35$	1.273	1.306	1.328	1.343	1.355
$w = 50$	1.327	1.357	1.376	1.389	1.399
$w = 75$	1.382	1.407	1.422	1.433	1.441
$w = 100$	1.415	1.437	1.450	1.459	1.466

5. Rotation of a prolate spheroid

When a rigid prolate spheroid is free to translate and rotate in an unbounded isotropic viscous fluid submitted to simple shear at infinity, the solution detailed by Jeffery [2] gives the rate of rotation of its long axis. The purpose of this Section is to evaluate this rotation when the fluid is orthotropic, since no analytical result is available, and to compare with the dumbbell model proposed in Section 2. In order to test the validity of this model, a few cases only are treated because the problem is defined by 9 parameters: the aspect ratio of the spheroid, its orientation with respect to the plane and direction of simple shear, the orientation of the principal axes of the second-order orientation tensor, two independent principal values of the latter, and the fiber volume fraction in the fluid surrounding the fiber considered (assuming all fibers have the same aspect ratios).

Fig. 6. The cubic volume (shown translucent) meshed for the study of the rotation of a tilted prolate spheroid (shown in light color). A simple shear is applied, which translates the upper and lower faces of the cube in opposite directions.

A mesh has been prepared, where a prolate rigid spheroid with a length of 20 and a diameter of 1 ($w = 20$) is embedded at the center of a cube of side 60. The mesh has been refined in the vicinity of the sharp ends of the spheroid, it has 427, 163 nodes, 311, 584 10-node quadratic tetrahedral hybrid elements, with a total of 1, 593, 076 unknowns. The sides of the cube are normal to the Cartesian axes and parallel to the symmetry planes of the fluid orthotropy, the long axis of the fiber is parallel to the (1,1,1) direction in order to avoid favoring an orthotropy axis (Fig. 6), and simple shear is applied in the X-direction parallel to the XZ-plane. The origin of the coordinate system is taken at the center of the cube and a velocity $v_X = \dot{\gamma} Y$, $v_Y = v_Z = 0$ is applied on all cube faces. In these conditions, the analytical solution of Jeffery [2] for an unbounded isotropic fluid domain gives the rotation rate of the unit vector parallel to the long axis **p** of the spheroid as

$$\dot{\mathbf{p}} = \mathbf{\Omega}\,\mathbf{p} + k\,\mathbf{D}\,\mathbf{p} - k\,(\mathbf{p}^T \mathbf{D}\,\mathbf{p})\,\mathbf{p} \qquad (25)$$

where $\mathbf{\Omega}$ and $\mathbf{D}$ are the antisymmetric and symmetric parts of the velocity gradient $\nabla\mathbf{v}$, respectively, and $k = (w^2 - 1)/(w^2 + 1)$, with (6) being recovered when $w \to \infty$ (extremely elongated spheroids). Eq. (25) leads to the following expressions for the components of $\dot{\mathbf{p}}$ in the case considered here:

$$\dot{p}_X = \frac{\dot{\gamma}}{\sqrt{3}}\left(\frac{1}{2} + \frac{k}{6}\right), \qquad \dot{p}_Y = \frac{\dot{\gamma}}{\sqrt{3}}\left(-\frac{1}{2} + \frac{k}{6}\right), \qquad \dot{p}_Z = -\frac{\dot{\gamma}}{\sqrt{3}}\frac{k}{3} \qquad (26)$$

which allows a validation of the finite element simulation. With the mesh described above, where $k = 0.995$ because $w = 20$, the three values of (26) have been recovered extremely precisely, with relative differences of less than 0.03%.

Because of the large value of k involved in the finite element model, the obtained rate of rotation is close to the value for $w \to \infty$, where $\dot{p}_X = -2\dot{p}_Y = -2\dot{p}_Z = 2\dot{\gamma}/(3\sqrt{3})$. Therefore, the components of $\dot{\mathbf{p}}$ obtained in the numerical simulations with an orthotropic fluid can be compared to the values given explicitly by the approximate dumbbell model (13) using the inverse drag tensor, namely:

$$\dot{p}_X = \frac{\dot{\gamma}}{\sqrt{3}}(1 - \xi_{XX}), \qquad \dot{p}_Y = -\frac{\dot{\gamma}}{\sqrt{3}}\,\xi_{YY}, \qquad \dot{p}_Z = -\frac{\dot{\gamma}}{\sqrt{3}}\,\xi_{ZZ} \qquad (27)$$

for a slender fiber tilted to the (1,1,1) direction with respect to the Cartesian axes. Note that in (27) the (X, Y, Z) axes are aligned with the principal axes of **a** (and, therefore, of ξ), but three cases arise when either $(X, Y, Z) = (1, 2, 3)$, or $(X, Y, Z) = (3, 1, 2)$, or $(X, Y, Z) = (2, 3, 1)$, leading to three different rotations of the fiber.

For instance, when the fluid surrounding the fiber contains a volume fraction $f = 0.3$ of fibers with an aspect ratio $w = 20$, two cases are considered, which correspond to points B and C in Fig. 4, i.e., where either $a_{11} = 1$ (aligned fibers) or $a_{11} = a_{22} = 1/2$. The following

Table 2
Components of $\dot{\mathbf{p}}$ given by the dumbbell model and by the finite element simulations for a spheroid with its long axis ($w = 20$) parallel to the $(1,1,1)$ direction and immersed in an orthotropic fluid (where $f = 0.3$ and $w = 20$, $a_{11} = 1$ in case B, $a_{11} = a_{22} = 1/2$ in case C) submitted to a simple shear. Three orientations of the fluid orthotropy with respect to the Cartesian axes are considered in each case.

(X, Y, Z)	Model	Case B			Case C		
		$\dot{p}_X/\dot{\gamma}$	$\dot{p}_Y/\dot{\gamma}$	$\dot{p}_Z/\dot{\gamma}$	$\dot{p}_X/\dot{\gamma}$	$\dot{p}_Y/\dot{\gamma}$	$\dot{p}_Z/\dot{\gamma}$
(1,2,3)	Spheroid	0.4888	−0.2448	−0.2440	0.4180	−0.1593	−0.2587
	Dumbbell	0.4790	−0.2395	−0.2395	0.4203	−0.1570	−0.2633
	Difference	−0.0098	0.0053	0.0045	0.0023	0.0023	−0.0046
(3,1,2)	Spheroid	0.3326	−0.0886	−0.2440	0.3188	−0.1612	−0.1576
	Dumbbell	0.3379	−0.0984	−0.2395	0.3141	−0.1570	−0.1570
	Difference	0.0053	−0.0098	0.0045	−0.0047	0.0042	0.0006
(2,3,1)	Spheroid	0.3318	−0.2455	−0.0863	0.4161	−0.2586	−0.1576
	Dumbbell	0.3379	−0.2395	−0.0984	0.4203	−0.2633	−0.1570
	Difference	0.0061	0.0060	−0.0121	0.0042	−0.0047	0.0006

values have been obtained with the finite element simulations reported in Section 4.2 for the components of the normalized inverse drag tensor: $\xi_{11} = 0.1704$ and $\xi_{22} = \xi_{33} = 0.4148$ in case B, $\xi_{11} = \xi_{22} = 0.2720$ and $\xi_{33} = 0.4560$ in case C. They lead to the values reported in Table 2 when the dumbbell model is applied. These results are compared in Table 2 with the rotations of the prolate spheroid given by the finite element simulations; they suggest that the dumbbell model evaluates the components of $\dot{\mathbf{p}}$ to within ± 0.01. This validates the assumption that the solution to the Jeffery problem in the anisotropic case can be approximated reasonably well by a dumbbell model.

The rotation rate predicted by Jeffery's equation for a slender fiber is recovered when $\xi_{XX} = 1/3$ in (27), and therefore a rotation towards the alignment of all other fibers (component $\dot{p}_{XX}$) is obtained faster or slower than predicted by Jeffery's equation when ξ_{XX} is smaller or larger than $1/3$, respectively. The values of $\dot{p}_{XX}$ predicted by (27) when using values of $\xi_{XX} < 1/3$ as obtained in Section 4.2 are confirmed by the finite element simulations shown above (Table 2), but they do not agree with the predictions of Koch and Shaqfeh [28]. The latter authors obtained $\dot{p}_{XX}$ values lower than given by Jeffery's equation by using a direct evaluation and summation of hydrodynamic effects to evaluate the rotation of a slender fiber when all other fibers immersed in the fluid are aligned in a given direction. Since our finite element simulations of a rotating fiber do not use the drag factor but merely rely on the preliminary evaluation of the effective behavior of the fluid surrounding the rotating fiber, we note that an agreement with Koch and Shaqfeh [28] might be obtained, at least qualitatively, with a different evaluation of the effective behavior that would lead to a slower rotation in the finite element simulations and to $\xi_{XX} > 1/3$ in Section 4.2. At the present stage, we may just observe that these two approaches, which are based on different evaluations of the effects of surrounding fibers in semi-dilute suspensions, lead to opposite trends. It may also be recalled incidentally that [28] is limited to aligned fibers, whereas our approach is more general.

6. Simulating the orientation kinematics of a population of rods

In this Section, the orientation kinematics of a population of initially randomly oriented rods is computed when the surrounding Newtonian fluid is submitted to a simple shear ($v_X = \dot{\gamma}Y$, $v_Y = v_Z = 0$, like in the previous Section). Two cases are considered, where the coupling of the rod orientation kinematics with the orientations of the surrounding rods is either ignored or taken into account. In the former no-coupling case, each rod evolves independently from the others, and its orientation history is obtained readily by integrating the standard Jeffery's Eq. (6). In the coupled case, the generalized Jeffery's Eq. (13) is used for evolving each orientation and, by contrast, the whole population of orientations must be updated at every time step.

At any time t in the integration procedure, the N rods involved in the numerical simulation of the suspension are described by their orientations $\mathbf{p}_i^t$ (with $i = 1, \cdots, N$), from which the second-order orientation tensor is computed as a discrete counterpart of (14):

$$\mathbf{a}^t = \frac{1}{N} \sum_{i=1}^{N} \mathbf{p}_i^t \otimes \mathbf{p}_i^t . \tag{28}$$

This tensor can then be used to compute the inverse drag tensor ξ^t at time t through (24), and finally (13) is applied to each rod in the population to obtain its rate of rotation $\dot{\mathbf{p}}_i^t$ in order to update the orientations with a mere explicit Euler scheme: $\mathbf{p}_i^{t+\Delta t} = \mathbf{p}_i^t + \Delta t\, \dot{\mathbf{p}}_i^t$ for $i = 1, \cdots, N$. The next time step can then be handled. This procedure is noticeably simplified by the use of the appropriate, preliminarily fitted, and constant σ value in (24), which can be read from Table 1 when the aspect ratio w of the fibers and their volume fraction f have been defined. Since the rods considered in this discrete approach do not have a finite diameter (hence an infinite aspect ratio and a zero volume), the fiber volume fraction and aspect ratio are present through the value of σ only. This explains why the simulations described below use the same set of N rods when different f and w values are considered. Neither f nor w affects the predictions of the uncoupled model, of course, since they are not present in (6).

A population of $N = 5,000$ rods is considered, with orientations which are initially distributed randomly and uniformly on the unit sphere, so that an almost isotropic orientation distribution is depicted. Since the rods are expected to orient along the shear direction (X-axis) because both (6) and (13) predict $\dot{\mathbf{p}} = \mathbf{0}$ if all fibers are aligned along this direction, the associated a_{XX} component of the orientation tensor should approach the value of 1 at long times. This quantity is plotted in Fig. 7 (where $\dot{\gamma} = 1 \text{ s}^{-1}$ has been used) as predicted by the standard Jeffery model and by the coupled model that takes into account the anisotropic effective medium. The predictions of the latter model depend on the fiber volume fraction and aspect ratio, and three cases are considered: $f = 0.10$ and $w = 20$, where $\sigma = 1.182$ applies according to Table 1, $f = 0.20$ and $w = 20$ ($\sigma = 1.242$) to demonstrate the effect of the volume fraction, $f = 0.20$ and $w = 50$ ($\sigma = 1.376$), to illustrate the influence of the aspect ratio. Of course, the orientation distribution is the same ($a_{XX} = 1/3$) in all cases initially and tends to be the same ($a_{XX} = 1$) at large times, but Fig. 7 shows that significant differences can be observed at intermediate times, although all curves are still very close to each other at small times. At any time, the orientation is more pronounced (less isotropic) with the coupled model than with the standard Jeffery prediction. Fig. 7 also shows that an increase in the fiber volume fraction tends to increase a_{XX}, but this effect is moderate (the curve for $f = 0.30$ and $w = 20$, not shown for clarity, would be very close to the $f = 0.20$ and $w = 20$ curve), whereas an increase of the fiber aspect ratio increases a_{XX} more strongly. Thus, for shear flows of fiber-
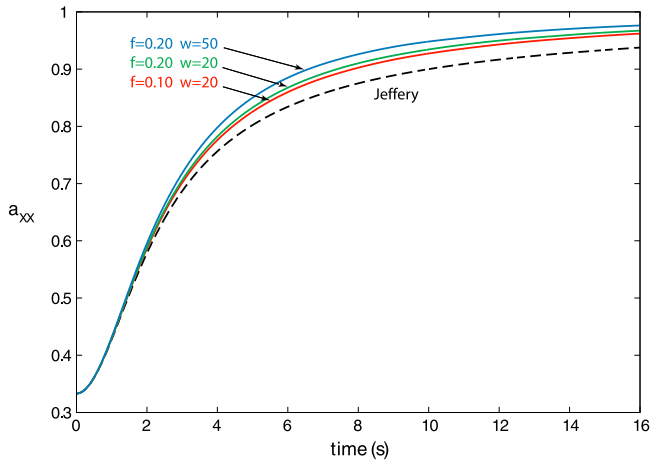
Fig. 7. Time evolution of the a_{XX} component of the orientation tensor when simple shear is applied along the X-axis (with $\dot{\gamma} = 1 \text{ s}^{-1}$) and the effective anisotropic fluid is either accounted for (solid lines) or ignored (standard Jeffery prediction, dashed line). Three combinations of fiber volume fractions f and aspect ratios w are considered, as indicated.

filled polymers, noticeable differences can be obtained in the final orientation state if the flow implies a significant anisotropy and if the total applied shear is not enough for reaching the fully aligned terminal state.

7. Concluding remarks

A model has been proposed, where the evolution of the orientation of each fiber is coupled to the orientations of the surrounding fibers in the flow of a fiber-filled fluid and includes the effects of the fiber volume fraction and aspect ratio. This has been performed by accounting for the effective behavior of the fiber-filled fluid, which is anisotropic although the fibers are embedded in an isotropic Newtonian fluid. The rotation of a fiber in these conditions could be predicted by using a dumbbell model, which allowed an extension of Jeffery's equation to anisotropic cases. This involved the numerical evaluation of the drag force applied on a sphere in an orthotropic incompressible fluid, and a simple fit has been proposed for its practical use in the coupled model. The assumed equivalence between the rotations of a fiber and of a dumbbell in a anisotropic fluid has been validated directly by finite element simulations. This work calls for the following remarks:

(i) The proposed model relies on some important assumptions. First, an effect of the fibers surrounding a given fiber is accounted for, but merely through the anisotropy they induce, not by the direct interactions they may have with the fiber considered. In other words, fiber-to-fiber contacts are neglected here, and this may be acceptable in two cases: when the fiber volume fraction is not too large, and when the fibers are sufficiently aligned (a decrease of the number of contacts has been observed by Mezher et al. [29], for instance). The first condition is closely related to the limit where the Mori-Tanaka model used here is reliable, so that large fiber volume fractions should be considered cautiously, and other homogenization models may be preferred in such cases. The second circumstance is increasingly likely to occur when the orientation distribution moves away from the isotropic case. Fortunately, this is rapidly obtained in simple shear with the coupled model.

(ii) The use of the fitted coefficient σ, as proposed in Section 4.2, is convenient in practice, because it leads to a simple and fast application of the coupled model, but it may give a crude approximation of the drag tensor in some circumstances, as illustrated in Fig. 5b. A direct use of the whole set of computed values of the drag tensor (obtained with some uncertainty through a numerical simulation, though) might be more satisfactory, but this

would lead to a more complex scheme. In particular, the drag tensor would have to be updated at each time step, because the orientation tensor evolves, whereas σ is constant. This might be performed with a suitable interpolation procedure using the results of the finite element simulations.

(iii) For practical reasons, the numerical simulation of the injection of fiber-filled polymers relies on the second-order orientation tensor to condense the orientation distribution function. As mentioned in Section 3, this has the consequence that the effective behavior of the fiber-filled fluid is orthotropic, which simplifies the evaluation of the drag tensor (reduced to 3 finite element simulations). In general, complex, flows of fiber-filled fluids, the orientation distribution function may not have three orthogonal symmetry planes, and the effective behavior would not be orthotropic, but of a more general anisotropy type instead. In these conditions, the numerical evaluation and tabulation of the drag tensor would be a formidable task.

(iv) The fiber aspect ratio appears at two places in the present coupled model. First, it has a strong effect on the effective anisotropic behavior of the fiber-filled fluid, as shown in Section 3, especially through the elongational viscosity of the reference unidirectional case. The effects induced on the drag tensor have been taken into account in this study, and they are reflected by the variations of σ in each column of Table 1. The aspect ratio comes also into play through coefficient k in the general Jeffery equation (25), but it is missing in (13), where an infinite aspect ratio is assumed. This is justified by the negligible effect of w in (25) when reasonably large values are used, as shown in Section 5, and by the next point below.

(v) A tri-dumbbell model has been proposed in [3], which reproduces Jeffery's equation for a general ellipsoid in an isotropic fluid, and we explored its extension to the present context of an anisotropic fluid like we did for the simple dumbbell in Section 2, in order to account for a finite aspect ratio. This involved extremely complex analytical expressions (not reported here) with, finally, numerical values for reasonably large aspect ratios very close to the predictions of the considerably simpler mono-dumbbell model used in the present paper.

(vi) There is no two-dimensional analog to the effect of anisotropy described in this paper. In such a simplified case, one would consider a distribution of orientations along the unit circle rather than on the unit sphere. This might appear as an ideal simple test case, but taking into account the anisotropy of the fiber-filled fluid would have no effect at all, unfortunately. The fundamental reason is that the viscosities along the two principal axes of the orientation tensor would be equal, although the two principal values of this tensor can have different values (with their sum being equal to 1). This property of an incompressible two-dimensional fluid has been shown by Fletcher [30] and, as a result, the drag tensor (and its inverse) has its two principal values equal. In other words, the drag is isotropic in two dimensions. Actually, the equivalent to the Jeffery solution is available for a two-dimensional anisotropic problem: the rotation of a rigid ellipse is merely independent of the surrounding anisotropy, as shown in [30].

Supplementary material

Supple ntary material associated with this article can be found, in the online version, at doi:10.1016/j.jnnfm.2019.07.006.

References

[1] F. Chinesta, From single-scale to two-scale kinetic theory description of rods suspensions, Arch. Comput. Methods Eng. 20 (2013) 1–29.

[2] G.B. Jeffery, The motion of ellipsoidal particles immersed in a viscous fluid, Proc. R. Soc. Lond. A102 (1922) 161–179.

[3] E. Abisset-Chavanne, F. Chinesta, J. Férec, G. Ausias, R. Keunings, On the multi-scale description of dilute suspensions of non-brownian clusters composed of rods, J. Non-Newtonian Fluid Mech. 222 (2015) 34–44.

[4] M. Perez, A. Scheuer, E. Abisset-Chavanne, A. Ammar, F. Chinesta, R. Keunings, On the multi-scale description of micro-structured fluids composed of aggregating rods, Contin. Mech. Thermodyn. (2018) 1–13, doi:10.1007/s00161-018-0659-1.

[5] M. Perez, A. Scheuer, E. Abisset-Chavanne, F. Chinesta, R. Keunings, A multi-scale description of orientation in simple shear flows of confined rod suspensions, J. Non-Newtonian Fluid Mech. 233 (2016) 61–74.

[6] A. Scheuer, E. Abisset-Chavanne, F. Chinesta, R. Keunings, Second-gradient modelling of orientation development and rheology of dilute confined suspensions, J. Non-Newtonian Fluid Mech. 237 (2016) 54–64.

[7] E. Abisset-Chavanne, J. Férec, G. Ausias, E. Cueto, F. Chinesta, R. Keunings, A second-gradient theory of dilute suspensions of flexible rods in a newtonian fluid, Arch. Comput. Methods Eng. 22 (2015) 511–527.

[8] D. Borziacchiello, E. Abisset-Chavanne, F. Chinesta, R. Keunings, Orientation kinematics of short fibres in a second-order viscoelastic fluid, Rheol. Acta 55 (2016) 397–409.

[9] A. Scheuer, E. Abisset-Chavanne, F. Chinesta, R. Keunings, Microscopic modelling of orientation kinematics of non-spherical particles suspended in confined flows using unilateral mechanics, Comptes-Rendus Méca 346 (2018) 48–56.

[10] M. Grmela, A. Ammar, F. Chinesta, One and two-fiber orientation kinetic theories of fiber suspensions, J. Non-Newtonian Fluid Mech. 200 (2013) 17–33.

[11] R.B. Bird, H.R. Warner Jr, D.C. Evans, Kinetic theory and rheology of dumbbell suspensions with brownian motion, Adv. Polym. Sci. 8 (1971) 1–90.

[12] C.F. Curtiss, R.B. Bird, A kinetic theory for polymer melts. i. the equation for the single-link orientational distribution function, J. Chem. Phys. 74 (1981) 2016–2025.

[13] S.G. Advani, C.L. Tucker III, The use of tensors to describe and predict fiber orientation in short fiber composites, J. Rheol. 31 (1987) 751–784.

[14] T. Mori, K. Tanaka, Average stress in matrix and average elastic energy of materials with misfitting inclusions, Acta Metall. 21 (1973) 571–574.

[15] Y. Benveniste, A new approach to the application of mori-tanaka's theory in composite materials, Mech. Mater. 6 (1987) 147–157.

[16] C.L. Tucker III, E. Liang, Stiffness predictions for unidirectional short- fiber composites: review and evaluation, Compos. Sci. Technol. 59 (1999) 655–671.

[17] A.J. Beaussart, J.W.S. Hearle, R.B. Pipes, Constitutive relationships for anisotropic viscous materials, Compos. Sci. technol. 49 (1993) 335–339.

[18] D.H. Chung, T.H. Kwon, Invariant-based optimal fitting closure ap- proximation for the numerical prediction of flow-induced fiber orientation, J. Rheol. 46 (2002) 169–194.

[19] Abaqus, Dassault Systèmes Simulia Corporation, Providence, RI, USA, 2014.

[20] G.G. Stokes, On the effect of the internal friction of fluids on the motion of pendulums, Trans. Camb. Phil. Soc. 9 (1851) 8–106.

[21] D.C. Lin, N.A. Langrana, B. Yurke, Force-displacement relationships for spherical inclusions in finite elastic media, J. Appl. Phys. 97 (2005). 043510–1

[22] J. Schöberl, NETGEN an advancing front 2d/3d-mesh generator based on abstract rules, Comput. Visual. Sci. 1 (1997) 41–52.

[23] M. Gómez-González, J.C.d. Álamo, Flow of a viscous nematic fluid around a sphere, J. Fluid Mech. 725 (2013) 299–331.

[24] R.B. Bird, J.M. Wiest, Anisotropic effects in dumbbell kinetic theory, J. Rheol. 29 (1985) 519–532.

[25] J. Azaiez, Constitutive equations for fiber suspensions in viscoelastic media, J. Non-Newtonian Fluid Mech. 66 (1996) 35–54.

[26] R. Guo, J. Azaiez, C. Bellehumeur, Rheology of fiber filled polymer melts: role of fiber-fiber interactions and polymer-fiber coupling, Polym. Eng. Sci. 45 (2005) 385–399.

[27] J.S. Cintra Jr, C.L. Tucker III, Orthotropic closure approximations for the flow-induced fiber orientation, J. Rheol. 39 (1995) 1095–1121.

[28] D.L. Koch, E.S.G. Shaqfeh, The average rotation rate of a fiber in the linear flow of a semidilute suspension, Phys. Fluids A 2 (1990) 2093–2102.

[29] R. Mezher, M. Perez, A. Scheuer, E. Abisset-Chavanne, F. Chinesta, R. Keunings, Analysis of the folgar & tucker model for concentrated fibre suspensions in unconfined and confined shear flows via direct numerical simulation, Compos. Part A 91 (2016) 388–397.

[30] R.C. Fletcher, Deformable, rigid, and inviscid elliptical inclusions in a homogeneous incompressible anisotropic viscous fluid, J. Struct. Geol. 31 (2009) 382–387.